DBR Laser with Nondynamic Plasma Grating Formed by Focused Ion Beam Implanted Dopants

MYRA M. BOENKE, STUDENT MEMBER, IEEE, M. C. WU, SHYH WANG, FELLOW, IEEE, WILLIAM M. CLARK, JR., EUGENE H. STEVENS, AND MARK W. UTLAUT

Abstract—A *static* plasma grating has been demonstrated experimentally [1] in a large optical cavity FIB-DBR GaAlAs/GaAs laser diode. The grating is formed by implanting stripes of dopants with a focused ion beam (FIB). The dopants ionize to form periodic fluctuations in the carrier concentration which, through the Kramers–Kronig relations, form an index grating. A model of the grating strength for optimization of the laser design is developed and presented here. The computed results show that κ can be increased by more than an order of magnitude over the 15 cm^{-1} estimated experimentally. Therefore, FIB-DBR (or -DFB) lasers with performance comparable to that of conventional DBR (or DFB) lasers can be expected.

I. INTRODUCTION

GRATINGS in III–V semiconductor materials are the basis of single-mode laser sources for optical communications and play an important role as optical couplers in the expanding field of optoelectronic integrated circuits (OEIC's). The standard method of forming gratings in semiconductor waveguides is to etch into the guiding material and regrow over it material with a different index, forming a periodic fluctuation in the effective index of the waveguide. Usually the grating is first defined holographically [2] or by an electron beam [3] in a mask, such as exposed photoresist or polymers. The pattern is then transferred to the semiconductor by wet chemical etching or ion milling. Direct etching techniques not requiring a mask such as photoelectrochemical etching [4] have also been demonstrated.

The other type of grating widely used in semiconductors is formed dynamically by interfering two laser beams in the material. An excess of carriers generated at the periodic constructive interference points of the beams depresses the index due to the plasma effect. These dynamic gratings were first observed in semiconductors in 1969 [5] and were used to observe transient carrier behavior in GaAs as early as 1978 [6]. They have been widely studied and used to measure carrier properties in a wide variety of semiconductors [7].

Gratings play a crucial role in improving the performance of semiconductor lasers. DFB [8] and DBR [9] lasers have been shown to have improved mode stability as a function of time and temperature [10], superior dynamic singlemode operation [11], and reduced frequency chirp. A DBR laser with single-mode operation and good side mode suppression due to a new type of grating formed by focused ion beam (FIB) implanted stripes of dopants has recently been demonstrated [1]. The purpose of this paper is to model this grating to provide the information needed to optimize the implantation parameters and the laser structure.

The type of grating described here relies on a plasma grating but does not require active pumping by external lasers. Instead, the periodic fluctuation in the carrier concentration is created by 1000 Å wide stripes of dopant atoms implanted with a FIB at multiples of the Bragg period. In Section II the model used to relate the change in index due to the free carriers from the implanted dopants is outlined. Based on this model, the coupling coefficient of the grating is calculated in Section III. Both an analytical expression, which reveals the dependence of the coupling coefficient on several waveguide and implant parameters, and a more flexible numerical calculation are presented. The geometry and fabrication details though previously reported [1] are summarized in Section IV for convenience. Some results of the model are discussed in Section V as are some of the potential advantages of this new technology as it applies to fabrication and design of DBR and DFB lasers.

II. MODEL OF INDEX CHANGE

A. Free Carrier Distribution

When nonuniformly distributed donors ionize in semiconductors the generated electrons diffuse towards areas of lower concentration according to the charge continuity equation

$$\vec{J}_n = q\mu_n \vec{E} n + qD_n \nabla n \qquad (1)$$

Manuscript received September 30, 1988; revised December 6, 1988. This work was supported in part by the Newport Research Corporation and the Optical Society of America under a Newport Research Award, by Bell Communications Research, by Eastman Kodak, and by the National Aeronautics and Space Administration under Grant NAG-1-580.

M. M. Boenke, M. C. Wu, and S. Wang are with the Department of Electrical Engineering and Computer Science, University of California, Berkeley, CA 94720.

W. M. Clark, E. H. Stevens, and M. W. Utlaut are with Hughes Research Laboratories, Malibu, CA 90265.

IEEE Log Number 8927337.

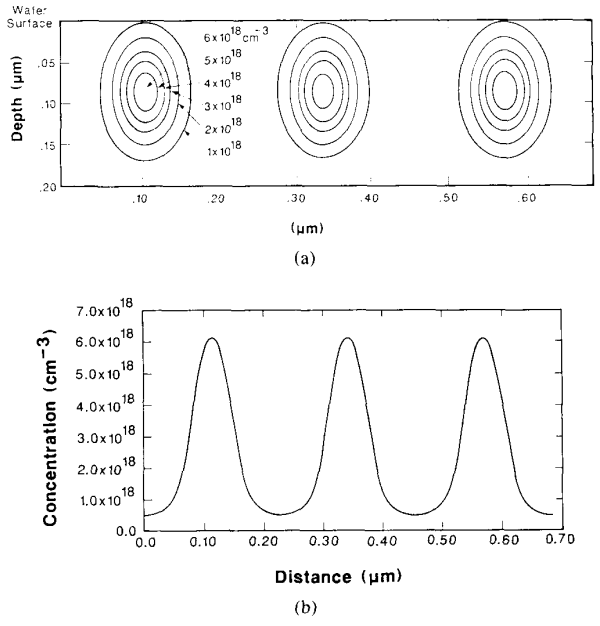

Fig. 1. (a) Computer simulation of the FIB-implanted stripes of Si in GaAs after a 950°C 10 s anneal. Contours of constant carrier concentration decrease in steps of 1×10^{18} cm^{-3} from peaks of 6.0×10^{18} cm^{-3} in the centers. (b) Free carrier concentration plotted across the peaks of (a) at the depth of 0.0850 μm.

where q is the electric charge, n is electron density, μ_n is carrier mobility, D_n is carrier diffusivity, and $\vec{E}$ is electric field. This leaves behind ionized donor atoms causing electric fields which oppose this diffusion current. The carriers and fields must also obey Poisson's equation

$$\epsilon \nabla^2 \psi = -q(p - n + N_D) \tag{2}$$

where N_D is the donor impurity concentration, ψ is potential and $-\nabla\psi = \vec{E}$. Equations (1) and (2) can be solved simultaneously [12] for the steady-state spatial distribution of the carriers.

Fig. 1(a) shows a two-dimensional cross section of the carrier concentration calculated using this approach for three FIB implanted stripes of dopants. The doping concentration is assumed to be a two-dimensional Gaussian with an implant depth of 0.0850 μm and standard deviation of 0.0442 μm. The horizontal standard deviation is determined by the resolution of the FIB beam, which has been measured to have a full width at half maximum of 700 Å. Further spreading due to the diffusion during the 10 s anneal at 950°C is negligible for Si_3N_4 capped Si implants in GaAs [13]. The peak dopant concentration is assumed to be 6.3×10^{18} cm^{-3}, with a background concentration of 5×10^{17} cm^{-3}. The surface of the wafer is towards the top of the figure. The lines show contours of constant carrier concentration spaced by 1.0×10^{18} cm^{-3}. In comparison, plots of the doping concentration are almost identical, so the carriers diffuse only a very small distance. Based on this result, the location of the carriers is approximated by the doping distribution for this model.

B. Relation of Index to Free Carriers

A large body of work has been done to model, calculate, and measure the change in absorption, and through the Kramers–Kronig relations, the change in index of GaAs near the band edge due to the free carriers [14], [15]. Calculations show that the index in GaAs below bandgap increases slightly with carrier concentration up to a concentration of about 6×10^{17} cm^{-3}. Above this, there is a linear relation between index and carriers of $\delta n/\delta N = -1.0 \times 10^{-20}$ cm^3. This linear relationship will be applied to GaAlAs in Section III to relate the change in index, and therefore the strength of the grating, to the change in carrier concentration caused by the FIB implants.

Fig. 1(b) shows the variation of the carrier concentration at a depth of 0.0850 μm across the peaks of the implanted stripes from Fig. 1(a). There is a peak-to-valley variation in carrier concentration of about 6×10^{18} cm^{-3}. Assuming the relation between change in index and change in carrier density to be a factor of -1.0×10^{-20} cm^3 as discussed above, this corresponds to an index variation of 0.06, which is the same order of magnitude as the change in index used in conventional etched gratings.

III. Coupling Coefficient

The coupling coefficient is a quantitative measure of the effectiveness of a grating and is given by [16]

$$\kappa = \frac{k_0^2}{2\beta N^2} \int_{-\infty}^{+\infty} \Delta[n(x, z)^2] E(x)^2 \, dx \tag{3}$$

where κ is the coupling coefficient, k_0 is the free-space wavenumber, β is the propagation constant in the medium, E is the y- (transverse) component of the fundamental E-field in the unperturbed guide, z is the direction of propagation, x is the direction of implant into the guide, and N^2 is a normalization constant given by

$$N^2 = \int_{-\infty}^{+\infty} E(x)^2 \, dx. \tag{4}$$

The form of the fundamental mode in the waveguide layer of a general three layer dielectric waveguide is

$$E = A \cos\left[k_g(w/2 + x_{\text{mode}})\right] e^{\gamma_1(x + w/2)} \quad (x \le -w/2) \tag{5a}$$

$$E = A \cos\left[k_g(x - x_{\text{mode}})\right] \quad (-w/2 \le x \le w/2) \tag{5b}$$

$$E = A \cos\left[k_g(w/2 - x_{\text{mode}})\right] e^{\gamma_3(x - w/2)} \quad (w/2 \le x) \tag{5c}$$

where k_g is the mode propagation constant and x_{mode} is the offset of the peak of the mode from the center of the guide, as shown in Fig. 2. Both of these parameters depend on the geometry of the particular waveguide. Fig. 3 illustrates the overlap of the mode with the grating. Three Gaussian curves are shown to indicate a series of two-

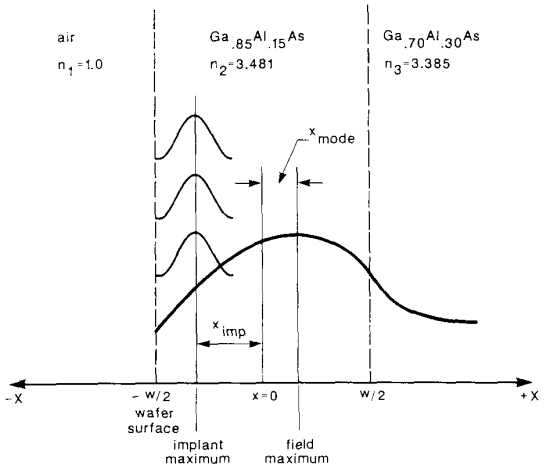

Fig. 2. Diagram of the model used to calculate the mode in the passive waveguiding section. The Gaussian spread in depth of three implanted stripes is indicated; the stripes actually continue along the length of the waveguide, spaced by 2288 Å. The distances from the center of the guide to the peak of the implant and to the peak of the mode are defined as $x_{implant}$ and x_{mode}, respectively.

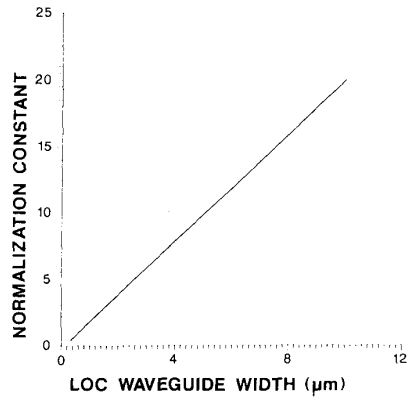

Fig. 3. The normalization parameter N^2 as defined in (4) as a function of guide width. N^2 increases monotonically with w, causing κ to decrease as the mode is spread out and overlaps less with the grating.

mensional Gaussian distributions in the propagation direction.

A. Analytical Solution

For implant doses below the rapid thermal annealing saturation limit as those modeled in Fig. 1(a), the carrier concentration closely follows the two-dimensional Gaussian shape of the implanted ion concentration. For this reason, a two-dimensional Gaussian which is periodic in the z-dependence is assumed here

$$\Delta n = (-1.0 \times 10^{-20}\ \mathrm{cm}^3) P_{cc} \left[\exp\left(\frac{-(x - x_{implant})^2}{2\sigma_x^2} \right) \right] \cdot \sum_{l=-\infty}^{l=+\infty} \exp\left(\frac{-(z - lp)^2}{2\sigma_z^2} \right) \quad (6)$$

where P_{cc} is the peak carrier concentration in cm^{-3}, σ_x and σ_z are the standard deviations of the implant after annealing in the x- (depth) and z- (propagation) directions, respectively, $x_{implant}$ is the distance from the peak of the implant to the center of the guide, and p is the period of the FIB stripes as indicated in Fig. 3. These values all depend on the ion, substrate, and implant energy used and on the time and temperature of the anneal. Noting that $\Delta[n(x)^2] \approx 2n\Delta n$, (5), and (6) can be substituted into (3) and integrated [17], giving

$$\kappa = \frac{k_0^2 n}{\beta N^2} (-1.0 \times 10^{-20}\ \mathrm{cm}^3) P_{cc} \cdot \sqrt{\frac{\pi}{2}}\, \sigma_x \left[e^{-k_g^2 \sigma_x^2} \cos\left[2k_g (x_{implant} - x_{mode}) \right] + 1 \right] \cdot \sqrt{\frac{\pi}{2}}\, \sigma_z \frac{1}{p} e^{-(m\pi/p)^2 2\sigma_z^2} \quad (7)$$

for the mth Fourier component in the z-direction.

This expression shows several dependencies for κ. First, in the x-direction, κ is proportional to the amount of ions implanted, determined by the peak concentration P_{cc}. Also, κ is at a maximum when there is maximum overlap between the guided mode and the grating, i.e., when $x_{implant} = x_{mode}$. However, this overlap term falls off exponentially with increasing σ_x^2 because as the profile of the implant becomes more flat, the position of its peak relative to the peak of the mode becomes much less significant, allowing the constant term to dominate. κ is also proportional to σ_x since a broader implant profile allows more overlap. The result is a maximum of κ as a function of σ_x when these two opposing effects are balanced.

The z-dependence is proportional to σ_z and is inversely proportional to $e^{\sigma_z^2}$, indicating a maximum κ for some value of σ_z which gives the maximum overlap of the mth Fourier component of a series of Gaussians spaced by period p.

Additional effects of the waveguide geometry are contained in the N^2 normalization factor. Fig. 3 shows that N^2 increases monotonically with w, causing κ to approach zero as the waveguide widens.

B. Numerical Solution

The above closed form solution assumes complete activation of the dopants. In practice, there is an upper limit to the activation level that can be achieved with rapid thermal annealed ion implantation. The percentage of the implanted ions that are activated decreases as this limit is approched [18]. For the FIB-DBR laser, Si, an amphoteric dopant which tends to compensate itself at high-doping levels was used. This could actually cause a decrease in free-carrier concentration near the peaks of the implants. Also, since FIB implantation is done at 0° tilt to maintain the focus, channeling may occur, although the effects are small in ⟨100⟩ GaAs [19]. In order to study these effects, a computer simulation was developed to integrate (3) numerically so that the expression for Δn in (6) could be modified arbitrarily.

For this model, the carrier concentration is assumed to be a flattened two-dimensional Gaussian related to the implant profile by a fixed activation percentage and clipped at an upper saturation limit. For rapid thermal annealed Si^{++} in GaAs, this limit has been observed [20] to be 6×10^{18} cm^{-3}. In the x-direction, the peak is shifted into the wafer by 33 percent and an exponential tail of slope -2.2 decade/μm starting at 25 percent of the maximum is added to account for channeling [19].

The FIB-DBR laser has a 0.5 μm thick guiding layer of $Ga_{0.85}Al_{0.15}As$ with air above and $Ga_{0.70}Al_{0.30}As$ below. Based on these compositions, n_1, n_2, and n_3 for the three regions shown in Fig. 2, are assumed to be 1.0, 3.481, and 3.385, respectively. These parameters give an x_{mode} as defined in Fig. 2 of 0.073 μm for the measured lasing wavelength of 8530 Å.

For a 100 KeV implant of Si in GaAs LSS calculations [21] give an implant depth of 0.0850 μm and standard deviation of 0.0422 μm, which corresonds to a characteristic length of 0.0625 μm. The FIB beam width has been measured to be 700 Å, which gives a standard deviation of 0.0297 μm and characteristic length of 0.0420 μm. For these parameters, a dose of 8×10^{14} cm^{-2} results in a peak dopant concentration of 9.7×10^{19} cm^{-3}, which is well over the saturation limit of 6×10^{18} cm^{-3}, so significant saturation occurs for the nominal case considered here. Increasing the implant range by 33 percent to account for channeling gives a range of 0.1133 μm, and an $x_{implant}$ as defined in Fig. 2 of 0.1367 μm for a 0.50 μm wide guide. Also, a uniform background n-type doping concentration of 5×10^{17} cm^{-3} and a second-order grating with a period of 2288 Å were assumed.

Figs. 4–8 show the effects on κ of varying some of the parameters discussed above around the nominal value, which is indicated by an asterisk. The saturation level has the most significant effect for two reasons. A higher saturation level allows a larger difference in carrier concentration between the peak of the implant and the background doping level, which gives a larger Δn, and, from (3), a larger value of κ. This can be seen in Fig. 4(a), which shows κ as a function of the implant dose for four saturation levels of 3.0, 6.0, 10.0, and 20.0×10^{18} cm^{-3}. For high doses, where saturation has the largest effect, there is an order of magnitude difference in κ between the lowest and the highest saturation level shown. The second important way saturation affects κ is that it changes the shape of the nominally periodic Gaussian grating so that the second-order Fourier coefficient does not remain constant. In Fig. 4(a), as the dose is increased from below saturation, κ increases monotonically until saturation starts occurring at, for example, 1×10^{14} cm^{-2} for the 6×10^{18} cm^{-3} saturation level curve. At this point, the second-order coefficient starts to decrease, going through zero and changing sign as the periodic Gaussian profile is deformed. This gives κ a null at around 2.5×10^{14} cm^{-2}.

Fig. 4(b) also shows κ as a function of dose parametrized instead by four implant energies of 50, 100, 200, and 300 KeV. As in Fig. 4(a), κ increases with dose until saturation is reached, passing through a null before continuing to increase. What Fig. 4(b) emphasizes is that implant energy has much less of an effect on the coupling strength of the grating than the saturation level or the dose. Although increased energy causes more overlap of the grating with the guided mode by moving the peak of the implant closer to the peak of the mode and widening the spread of the implant, it also decreases the peak doping level which decreases Δn. These two effects have opposing influences on κ, as seen in (3). Consequently, all four curves are very close where saturation has little effect below about 1×10^{14} cm^{-2}. Only above 30×10^{14} cm^{-2}, well beyond the effect of the changing sign of the Fourier coefficient, does higher implant energy cause a significant increase in the value of κ.

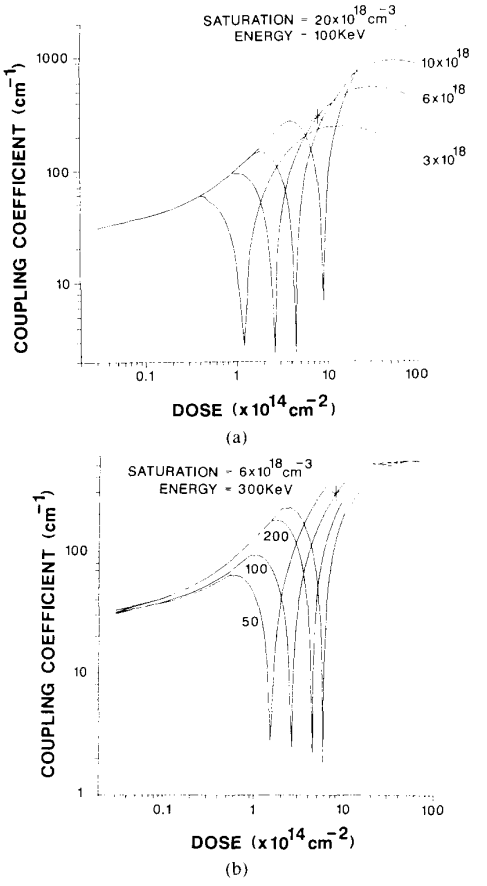

Fig. 4. Coupling coefficient as a function of implant dose for (a) rapid thermal annealed dopant activation saturation levels of 3, 6, 10, and 20 $\times 10^{18}$ cm^{-3} and (b) implant energies of 50, 100, 200, and 300 KeV. The nominal point used for the fabrication of the FIB-DBR is indicated by an asterisk.

The coupling strength is also very sensitive to the width of the FIB stripe, as shown in Fig. 5 for the same four saturation values used in Fig. 4(a). For a fixed dose, as the stripe width is increased from 0.0200 μm to 0.0800 μm, the dopants become more spread out, decreasing the peak doping level and therefore the amount of flattening due to saturation. As in the case of increasing dose in Fig. 4, the Fourier coefficient goes through a zero, causing a null in κ at some point. For larger values of characteristic

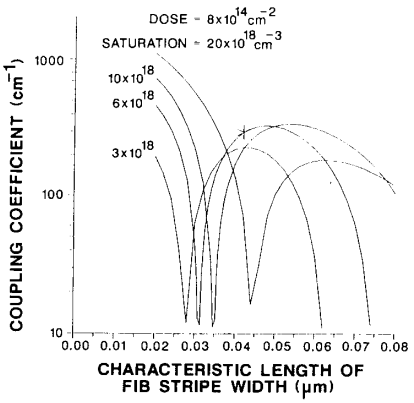

Fig. 5. Coupling coefficient as a function of characteristic length of the free carriers in the guiding (z-) direction (characteristic length = $\sqrt{2}\times$ standard deviation) for rapid thermal annealed dopant activation saturation levels of 3, 6, 10, and 20 $\times$ 10^{18} cm^{-3}. The nominal point used for the fabrication of the FIB-DBR is indicated by an asterisk.

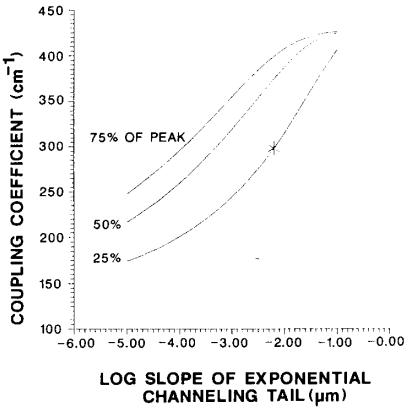

Fig. 7. Coupling coefficient as a function of the exponent (in decades/μm) of the exponential tail added to the implanted dopant distribution to account for channeling. The tail starts at the peak of the implant and extends into the wafer from there. The concentration assumed at the start of the tail is taken as 25, 50, and 75 percent of the peak concentration for the three curves shown, respectively. The nominal point used for the fabrication of the FIB-DBR is indicated by an asterisk.

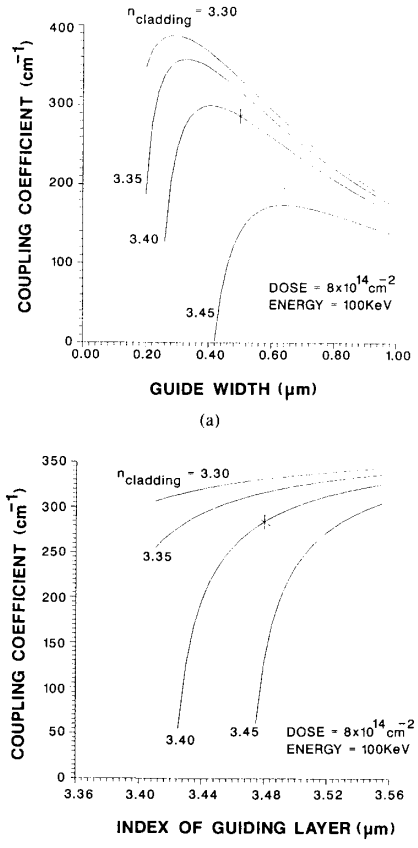

Fig. 6. Coupling coefficient as a function of (a) thickness and (b) index of the LOC waveguiding layer for cladding layer indexes of 3.30, 3.35, 3.40, and 3.45. The nominal point used for the fabrication of the FIB-DBR is indicated by an asterisk.

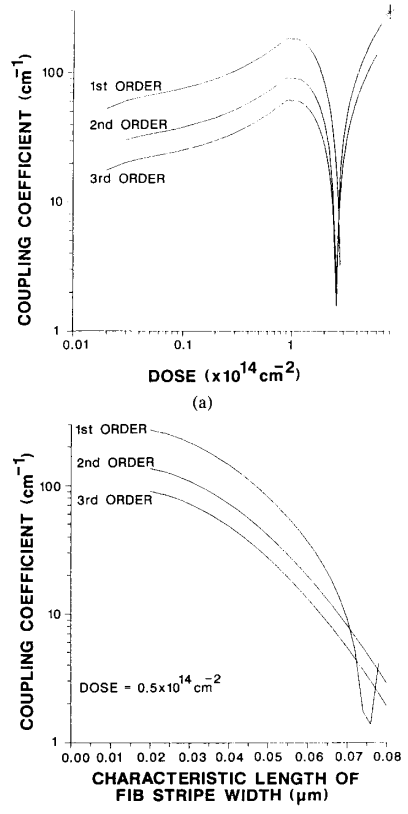

Fig. 8. Coupling coefficient as a function of (a) dose and (b) FIB stripe width for first-, second-, and third-order gratings. The nominal point used for the fabrication of the FIB-DBR is indicated by an asterisk.

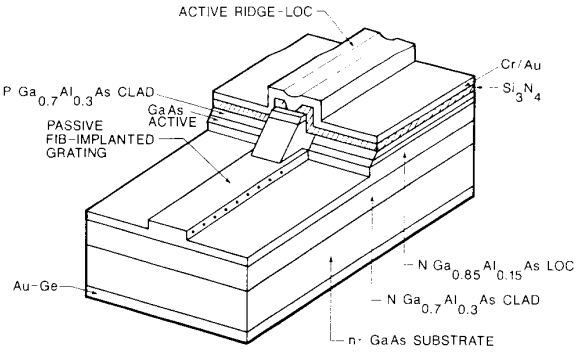

Fig. 9. Schematic diagram of the FIB-DBR. The active region is a large optical cavity buried heterostructure ridge waveguide. The passive section is etched down to the waveguide below the active region so that the FIB grating could be directly implanted into the waveguide.

length the stripes slur together, causing κ to decline after reaching a peak.

The waveguide structure is also important to achieving high coupling efficiency. Fig. 6(a) and (b) show the effect of the waveguide width and index, respectively, for cladding layer indexes of 3.30, 3.35, 3.40, and 3.45. For each cladding index, there is an optimum guide width to bring the mode toward the surface of the guide for maximum overlap of the field with the grating. If the guide is too narrow, the mode is not guided and for wider guides the mode is spread out and further from the surface. Lower values of the cladding index allow a larger difference with the guiding layer index, and therefore tighter confinement. Fig. 6(b) shows that the guiding layer index can become critical if the cladding layer index is not low enough.

The effect of variation in the slope (in decades/μm) of the exponential tail in the carrier concentration profile due to channeling is plotted in Fig. 7 for magnitudes relative to the peak carrier concentration of 25, 50, and 75 percent. In the case of the FIB grating, channeling is not detrimental because it effectively increases the implant range and spread and therefore the overlap of the grating with the mode. A less negative slope means deeper penetration of the dopants resulting in higher values of κ.

The coupling coefficients of first- and third-order gratings are shown for comparison as a function of dose and FIB stripe width in Fig. 8(a) and (b), respectively.

IV. Experimental Results

A. Geometry

Fig. 9 shows the structure of the laser used to demonstrate the FIB grating [1]. It is basically a ridge waveguide large optical cavity (LOC) GaAs laser with a 0.5 μm thick LOC layer of $Ga_{0.85}Al_{0.15}As$ and $Ga_{0.70}Al_{0.30}As$ cladding layers. One end of the ridge was selectively etched down to the LOC guiding layer, forming a passive section and allowing implantation directly into the guide. A second-order grating was used so that grating action could be determined either from single-mode lasing or from light emission normal to the surface. After implantation Si_3N_4 was deposited as a cap for the rapid thermal anneal of the implant and as a mask to etch a 0.1 μm high ridge in the LOC layer to provide some lateral confinement. Standard contacts were evaporated and the wafer was lapped and cleaved.

B. FIB Implantation

The implantations were produced by scanning the FIB from a three lens, mass separating, variable energy ion focusing column [22]. The dose is controlled by changing the number of repetitive scans by the beam over the stripe. In calculating the number of scans required, the stripe width was assumed to have the profile of the beam, which has a Gaussian current density profile with a 700 Å full width at half maximum. This corresponds to a standard deviation of 0.0420 μm. System accuracy for beam placement is estimated to be within 450 Å. The gratings were implanted at 100 KeV with a second-order period of 2288 Å and were annealed at 950°C for 10 s with a thermal Si_3N_4 cap.

C. Measurements

Fig. 10 shows the laser's spectrum at temperatures ranging from 16.8 to 42.1°C. Above about 20°C the DBR mode is dominant. No mode hopping is seen and an average wavelength shift of 0.8 Å/°C is observed. Fig. 11 shows light emission from the surface of the laser. Peaks of scattered light are seen at each facet and, due to a large mode mismatch between cavities, at the cavity interface as well. However, a substantial amount of light, which decreases roughly exponentially, is also seen over the grating section. This exponential drop can be used to estimate [1] the grating coupling coefficient, which is defined in (3), to be about 15 cm^{-1}.

V. Discussion

A. Device Optimization

The above numerical calculations are encouraging because they predict a coupling coefficient of nearly 300 cm^{-1} for the FIB-DBR laser which is comparable to or exceeds the level of coupling in conventional DBR lasers [10] and they indicate several aspects in which the design can be optimized to increase κ even further. There are several possible reasons why a coupling coefficient of this magnitude was not observed experimentally [1]. As indicated in Fig. 5, κ is very sensitive to the FIB stripe width. The fineness of the FIB stripe makes measuring the standard deviation difficult. Conventional methods of measuring a stripe etched or milled by the beam do not necessarily correspond to the $1/e$ width of the beam (i.e., twice the standard deviation) and resolution measurements must be done with the same energy and ion as the implant to be accurate. The characteristic length of 0.0420 μm assumed in the model was calculated using resolution

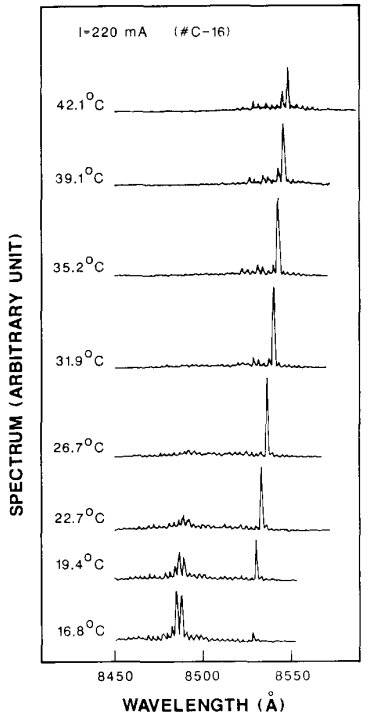

Fig. 10. Spectra of the FIB-DBR as a function of temperature. Good side mode suppression is observed from 20 to 35°C. The DBR mode shifts by 0.8 Å/°C.

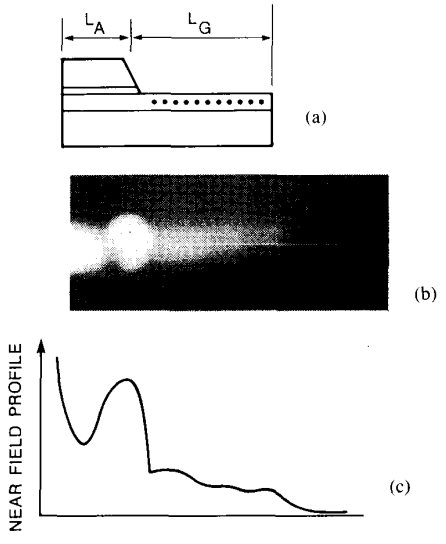

Fig. 11. Surface light emission of the FIB-DBR. (a) Schematic cross section to scale with measurements. (b) Streak camera picture of near field. (c) Intensity profile along center of guide.

measurements at high beam voltages which give the tightest focus. The actual FIB-DBR grating implant was done at a lower voltage which could have resulted in a significantly broader beam width. Lateral scattering of the ions in the GaAlAs before coming to rest could also contribute to the FIB stripe characteristic length. Further, although it has been shown that a Si_3N_4 cap reduces diffusion during annealing [13] to a level that is insignificant for the 10 s rapid thermal anneal used on the FIB grating, it was not possible to measure how much diffusion actually occurred. From Fig. 5, the experimentally measured κ of 15 cm^{-1} is the result of a characteristic length of 0.073 μm. Assuming some of these effects occurred in the fabrication of the FIB-DBR, optimization of the implant energy and annealing conditions to reduce the FIB stripe width should increase κ by over an order of magnitude.

A second factor which could have reduced κ is the shape of the periodic function. This model assumes an abruptly truncated Gaussian as a first-order approximation. Actually, the carrier concentration will smoothly approach the saturation level. Since the location of the null caused by the second-order Fourier coefficient going through zero is dependent on the shape of the function, it is possible that the FIB-DBR was closer to a null than the simulation indicates in Fig. 5.

Another means of increasing κ is to use an n-type dopant which can be activated to higher concentrations since the change in index is directly proportional to the carrier concentration in (6). Also, some p-type dopants such as Zn can be activated to 1 to 2 $\times$ 10^{19} cm^{-3}.

The waveguide structure is also important to achieving good overlap of the grating with the guided mode and therefore, high coupling efficiency. It must be designed to keep the mode as close to the surface as possible. The waveguide structure in the FIB-DBR [1] was not designed for optimum overlap with the grating. Fig. 6(a) shows that by increasing the Al content of the cladding layer to reduce the index closer to 3.30 and reducing the guide width to 0.3 μm, κ can be increased by 50 percent. Since the mode overlap has an independent effect on κ from the Fourier coefficient, this increase would be in addition to the increases obtained from optimizing the FIB stripe width.

A further improvement in coupling strength and therefore singlemode characteristics would be to use a first-order grating. Fig. 8(a) compares the coupling strengths of first-, second-, and third-order gratings. First-order gratings have a larger κ by about a factor of two for doses below the point that significant saturation occurs. First-order gratings are no more sensitive to the FIB stripe width than higher order gratings at these low doses, as shown in Fig. 8(b) for a dose of 0.5 $\times$ 10^{14} cm^{-2}.

B. Advantages of the FIB Grating

The FIB grating has potential uses other than in FIB-DBR lasers. Calculations of dopant diffusion at growth temperatures indicate it should be possible to regrow over the grating to bury it in the active region of a DFB laser. First-order gratings in InGaAsP DFB lasers are possible. Improved crystal quality could be achieved in DFB lasers fabricated in molecular or chemical beam epitaxy systems with a FIB attached because the wafer need not be exposed to masking materials, etchants, and atmospheric pressure during mid-growth. FIB gratings could also be used as off-chip couplers for OEIC's or on-chip couplers between optical devices. Since they are written locally by computer control, FIB gratings can be used at many different angles or written at different periods on the same wafer making multiple on-chip coupling and multi-fre-

quency laser arrays easily realizable. Furthermore, curves or chirped gratings are possible.

The versatility of the FIB implanter has been previously demonstrated in semiconductor electronic device fabrication including MESFET's with a striped channel structure [23] and laterally profiled active area implants to reduce the Kirk effect in bipolar transistors [24]. In semiconductor lasers FIB implants have been used to disorder superlattices [25] and FIB-micromachining has been utilized to provide facet etching for coupled cavity lasers [26], and laser arrays [27]. Disordering and etching, however, require long FIB processing times and do not emphasize the flexible advantages of this new fabrication tool. The plasma grating is achieved with at least an order of magnitude shorter write times. Because of this, the FIB grating has the potential to become an important application of FIB technology to optoelectronic device fabrication in the future.

VI. Conclusion

In summary, we have demonstrated a new principle for function of nondynamic gratings in semiconductor devices based on the plasma effect. The grating was demonstrated in a GaAs/GaAlAs FIB-DBR laser which showed stable single-mode operation over a 20°C temperature range with only 0.8 Å/°C shift in wavelength. Simulations show that FIB-implanted dopant stripes ionize to form a carrier grating balanced by the fields from the resulting space charge. Calculations show that of all the waveguide geometry and implant parameters, κ depends most strongly on the implant activation saturation level, the standard deviation in the z-direction, and dose. Optimization of the implant parameters could increase κ by over an order of magnitude over the value of 15 cm^{-1} estimated from surface emission from the second-order grating.

References

[1] M. C. Wu, M. M. Boenke, S. Wang, W. M. Clark, Jr., E. H. Stevens, and M. W. Utlaut, "GaAs/GaAlAs distributed Bragg reflector laser with a focused ion beam, low dose dopant implanted grating," *Appl. Phys. Lett.*, vol. 53, no. 4, pp. 265-267, July 25, 1988.

[2] A. Labeyrie and J. Flamand, "Spectrographic preformance of holographically made diffraction gratings," *Opt. Commun.*, vol. 1, no. 1, pp. 5-8, Apr. 1969.

[3] S. Okazaki, F. Murai, O. Suga, H. Shiraishi, and S. Koibuchi, "A practical electron beam direct writing process technology for submicron device fabrication," *J. Vac. Sci. Technol.*, vol. B5, no. 1, pp. 402-404, 1987.

[4] K. D. Cummings, L. R. Harriott, G. C. Chi, and F. W. Ostermayer, Jr., "Using focused ion beam damage patterns to photoelectrochemically etch features in III-V materials," *Appl. Phys. Lett.*, vol. 48, no. 10, pp. 659-661, Mar. 10, 1986.

[5] J. P. Woerdman and B. Bolger, "Diffraction of light by a laser induced grating in Si," *Phys. Lett.*, vol. 30A, no. 3, pp. 164-165, Oct. 6, 1969.

[6] C. A. Hoffman, K. Jarasiunas, and H. J. Gerritsen, "Measurement of surface recombination velocity in semiconductors by diffraction from picosecond transient free-carrier gratings," *Appl. Phys. Lett.*, vol. 33, no. 6, pp. 536-538, Sept. 15, 1978.

[7] A. Miller, D. A. B. Miller, and S. D. Smith, "Dynamic non-linear optical processes in semiconductors," *Advances Phys.*, vol. 30, no. 6, pp. 697-800, 1981.

[8] Y. Nakano and K. Tada, "Low threshold operation of a GaAlAs/GaAs distributed feedback laser with double channel planar buried heterostructure," *Appl. Phys. Lett.*, vol. 49, no. 18, pp. 1145-1147, Nov. 3, 1986.

[9] F. K. Reinhart, R. A. Logan, and C. V. Shank, "GaAs-$Al_xGa_{1-x}As$ injection lasers with distributed Bragg reflectors," *Appl. Phys. Lett.*, vol. 27, no. 1, pp. 45-48, July 1975.

[10] K. Kojima, S. Noda, K. Mitsunaga, K. Kyuma, and K. Hamanaka, "Continuous wave operation of a surface-emitting AlGaAs/GaAs multiquantum well distributed Bragg reflector laser," *Appl. Phys. Lett.*, vol. 50, no. 24, pp. 1705-1707, June 15, 1987.

[11] J. Glinski and T. Makino, "Yield analysis of second-order DSM DFB lasers and implications for design," *IEEE J. Quantum Electron.*, vol. QE-23, pp. 849-859, June 1987.

[12] A software package called PISCES™ which simultaneously solves charge continuity and Poisson's equations assuming bulk properties of either Si or GaAs was used for this simulation. PISCES™ is a registered trademark of Stanford Univeristy.

[13] T. Onuma, T. Hirao, and T. Sugawa, "Study of encapsulants for annealing Si-implanted GaAs," *J. Electrochem. Soc.: Solid-State Sci., Technol.*, vol. 129, no. 4, pp. 837-840, Apr. 1982.

[14] C. H. Henry, R. A. Logan, and K. A. Bertness, "Spectral dependence of the change in refractive index due to carrier injection in GaAs lasers," *J. Appl. Phys.*, vol. 52, no. 7, pp. 4457-4461, July 1981.

[15] M. Cross and M. J. Adams, "Effects of doping and free carriers on the refractive index of direct-gap semiconductors," *Opto-electron.*, vol. 6, pp. 199-216, 1974.

[16] A. Yariv, "Coupled-mode theory for guided-wave optics," *IEEE J. Quantum Electron.*, vol. QE-9, pp. 919-933, Sept. 1973.

[17] I. S. Gradshteyn and I. M. Ryzhik, *Table of Integrals, Series, and Products*. Orlando, FL: Academic, 1980. Apply the half-angle formula, then use integrals 3.923-2 and 3.321-3.

[18] K. Tabatabaie-Alavi, A. N. M. Masum Choudhury, and C. G. Fonstad, "Rapid thermal annealing of Be, Si, and Zn implanted GaAs using an ultrahigh power argon arc lamp," *Appl. Phys. Lett.*, vol. 43, no. 5, pp. 505-507, Sept. 1, 1983.

[19] R. G. Wilson and V. R. Deline, "Ion channeling in GaAs: Si, S, Se, and Te," *Appl. Phys. Lett.*, vol. 37, no. 9, pp. 793-796, Nov. 1, 1980.

[20] D. E. Davies, P. J. McNally, J. P. Lorenzo, and M. Julian, "Incoherent annealing of implanted layers in GaAs," *IEEE Electron Devices Lett.*, vol. EDL-3, pp. 102-103, Apr. 1982.

[21] J. F. Gibbons, W. S. Johnson, and S. W. Mylroie, *Projected Range Statistics*. Stroudsburg, PA: Dowden, Hutchinson & Ross, 1983.

[22] V. Wang, J. W. Ward, and R. L. Seliger, "A mass-separating focused-ion-beam system for maskless ion implantation," *J. Vac. Sci. Technol.*, vol. 19, no. 4, pp. 1158-1163, Nov./Dec. 1981.

[23] D. B. Rensch, D. S. Matthews, M. W. Utlaut, M. D. Courtney, and W. M. Clark, Jr., "Performance of the focused-ion-striped transistor (FIST)—A new MESFET structure produced by focused-ion-beam implantation," *IEEE Trans. Electron Devices*, vol. ED-34, pp. 2232-2237, Nov. 1987.

[24] R. H. Reuss, D. Morgan, A. Goldenetz, W. M. Clark, D. B. Rensch, and M. Utlaut, "Fabrication of bipolar transistors by maskless ion implantation," *J. Vac. Sci. Technol.*, vol. B4, no. 1, pp. 290-294, Jan./Feb. 1986.

[25] K. Ishida, K. Matsui, T. Fukunaga, J. Kobayashi, T. Morita, E. Miyauchi, and H. Nakashima, "Scan speed effects on enhanced disordering of GaAs-AlGaAs superlattices by focused Si ion beam implantation," *Appl. Phys. Lett.*, vol. 51, no. 2, pp. 109-111, July 13, 1987.

[26] R. K. DeFreez, J. Puretz, R. A. Elliott, J. Orloff, and L. W. Swanson, "CW operation of widely and continuously tunable micromachined-coupled-cavity diode lasers," *Electron. Lett.*, vol. 22, no. 17, pp. 919-921, Aug. 14, 1986.

[27] J. Puretz, R. K. DeFreez, R. A. Elliott, and J. Orloff, "300 mW operation of a surface-emitting phase-locked array of diode lasers," *Electron. Lett.*, vol. 23, no. 3, pp. 130-131, Jan. 29, 1987.

Myra M. Boenke (S'81-M'81-S'84) was born in Cleveland, OH, on March 25, 1959. She received the B.S. degree in electrical engineering from Cornell University, Ithaca, NY, in 1980 and the M.S.E. degree in electrical engineering from Princeton University, Princeton, NJ, in 1981.

She worked on system integration of the undersea fiber optic transAtlantic cable at Bell Laboratories from 1981 to 1983 and is presently working towards the Ph.D. degree at the University of California, Berkeley in the area of quantum electronics.

Ms. Boenke received the Newport Research Award from the Optical Society of America in 1987. She is a member of the Optical Society of America and the American Physical Society.

M. C. Wu, photograph and biography not available at the time of publication.

Shyh Wang (S'49-A'52-M'57-M'67-SM'74-F'78), photograph and biography not available at the time of publication.

William M. Clark, Jr. received the B.S. degree in 1958 from Stanford University, Stanford, CA, and the M.S. and Ph.D. degrees in 1966 and 1968, respectively, from the University of California, Berkeley, all in electrical engineering.

He has been with the Hughes Research Laboratories since 1973, and is currently head of the Focused Ion Beam Applications section that conducts research on the use of focused ion beams in in microelectronics and integrated optical device fabrication. He was formerly Assistant Professor of Electrical Engineering at the University of Texas at Austin, and performed research in quantum electronics and nonlinear optics.

Eugene H. Stevens is a senior development engineer at the Hughes Research Laboratories where for 13 years he has been responsible for the design, improvement, and operation of ion focusing equipment. Previously he performed research on flat TV tubes with Kaiser Research and associated firms and was a member of the U.S. Air Force.

Mark W. Utlaut received the B.S. degree in mathematics and physics from the University of Colorado, Boulder, and the Ph.D. degree in physics from the University of Chicago, Chicago, IL.

He is currently with the physics faculty, the Department of Physical and Life Sciences, University of Portland, Portland, OR. Formerly, he was a member of the technical staff at the Hughes Research Laboratories in Malibu, CA. His current interests are in quantum mechanics and solar astronomy.